Pushing and Rotating a Heavy Mass Rigid Body Using an Omnidirectional Aerial Manipulator

Hameed Ullah
Department of Electrical Engineering and Information Technology, University of Naples Federico II,
Naples, Italy.
ORCID: 0000-0002-4022-9657,
hameed.ullah@unina.it

Santos Miguel Orozco Soto
Science and Technology College, Autonomous University of Mexico City,
Mexico City, Mexico.
ORCID: 0000-0001-6191-4306
santos.orozco@uacm.edu.mx

Naveed Mazhar
Unmanned Vehicles Research Lab, DEE, CEME, National University of Sciences & Technology,
Islamabad, Pakistan.
ORCID: 0000-0001-7039-5368
naveed.mazhar@ceme.nust.edu.pk

Irfan Ahmad
Department of Automatic Control and Systems Engineering School of Bilbao, University of the Basque Country,
Bilbao, Spain
ORCID: 0000-0001-6075-2464
irfanahmad.irfan@ehu.eus

Vincenzo Lippiello
Department of Electrical Engineering and Information Technology, University of Naples Federico II,
Naples, Italy.
ORCID: 0000-0002-6089-2333
vincenzo.lippiello@unina.it

Fabio Ruggiero
Department of Electrical Engineering and Information Technology, University of Naples Federico II,
Naples, Italy.
ORCID: 0000-0001-7539-9157
fabio.ruggiero@unina.it

***Abstract*—This paper presents the pushing and rotation of a heavy rigid body using an omnidirectional actively tilted aerial manipulator, controlled via a hybrid force/position controller. Unlike conventional unmanned aerial vehicles, the proposed system enables precise horizontal force application, making it ideal for aerial physical interaction tasks. The hybrid controller is implemented in the Robot Operating System and validated through extensive simulations in a Gazebo physics-engine-based environment. The manipulator's performance was evaluated in two scenarios: circular trajectory tracking and the rotation of a heavy rigid mass. Results demonstrated its capability to follow complex trajectories with high accuracy and exert sustained forces for object manipulation. The system exhibited excellent stability and precision, underscoring its potential for real-world applications in challenging environments.**

***Index Terms*—Omnidirectional aerial manipulator, physical interaction, actively tilting multirotor, robust controller, pushing and rotating rigid body.**

I. Introduction

Traditionally, unmanned aerial vehicles (UAVs) have been employed for tasks such as aerial inspection, photography, and surveillance, proving indispensable in hazardous environments [1]–[4]. However, many of these tasks require direct physical interaction with the environment [5]–[9]. This need for aerial physical interaction (APhI) has led to the modification of UAVs into aerial manipulators, which combine UAV platforms with robotic arms or manipulators. The degrees of freedom (DoFs) of these manipulators, along with tip sensing and actuation capabilities, are tailored to the specific task. Aerial manipulators are now used in a range of APhI applications, including transportation, positioning, structure cleaning, object grasping, operating in hazardous areas, and tasks such as pushing and sliding objects.

To achieve the objectives in the aforementioned applications, aerial manipulators must be equipped with advanced sensing, actuation, and control capabilities. The integration of a manipulator with a UAV increases the system's complexity due to the dual challenges of controlling the manipulator and addressing the inherent under-actuation and stability issues of the UAV. Moreover, the force requirements in APhIs can vary significantly within a single task. For example, in firefighting, different levels of force may be needed to open a window in a large building compared to pushing a fire-damaged structure to prevent further ignition. Consequently, it is crucial for aerial manipulators to be equipped with a control framework capable of managing such active tasks while maintaining the stability of the overall system [6], [10].

A straightforward approach to managing the increased complexity of aerial manipulators is to provide separate control for the UAV's position and the manipulator for interaction tasks. In this approach, the UAV first reaches the desired position and orientation for APhI. Once in place, the manipulator controller begins the interaction to accomplish the task [5], [11]. This method reduces complexity by decoupling the control of the UAV and the manipulator. However, challenges related to the force exerted back onto the UAV remain. Additionally, the UAV must be capable of handling the forces imparted by the manipulator, and the aerial platform should offer intuitive

The research leading to these results has been supported by the AERO-TRAIN Project, European Union's Horizon 2020 Research and Innovation Program under the Marie Skłodowska-Curie Grant Agreement 953454. The authors are solely responsible for its content.

control for the human operator during APhI missions [8].

The selection of an appropriate UAV for aerial manipulation depends on the specific application [12]. For tasks such as pushing and rotating a static object, an actively tilted UAV is often preferred due to its ability to apply relatively higher forces and address the under-actuation problem inherent in UAVs [13]–[15]. Once the UAV is selected, the next challenge lies in designing a suitable controller, as the complexity increases with the inclusion of a tilting mechanism. A nonlinear model predictive control (NMPC) strategy for motion and force control of tilted UAVs is presented in [16]. Detection of pipe welds using articulated aerial manipulators is discussed in [17], while a second-order sliding mode controller for omnidirectional UAVs is used in [18]. For APhI tasks, impedance and direct force controllers are the most common approaches [19], [20]. These controllers manage the manipulator and are often combined with other control frameworks, such as nonlinear disturbance-observer-based robust controllers [21] and model predictive controllers [22]. For tasks involving interaction and pushing movable objects, a nonlinear disturbance-observer (DOB)-based robust controller has also been employed [21].

In this paper, we present a hybrid force/position control architecture for an omnidirectional, actively tilted aerial manipulator. This system leverages the tilting rotor's ability to exert controlled horizontal forces, enabling precise push-and-slide operations as well as the rotation of heavy rigid bodies. Unlike conventional UAVs, the proposed system integrates an actively tilting rotor mechanism, allowing for horizontal force application without compromising stability. The designed manipulator arm, combined with the control architecture, enables the system to exert several Newtons of force over extended durations, making it well-suited for interaction with heavy objects in a controlled manner. Trajectory tracking and object manipulation tasks were performed to validate the system's performance through simulations in Gazebo, demonstrating its effectiveness. The system is developed using C++ and Python, with communication facilitated by the Robot Operating System (ROS) middleware. Experiments were conducted in the Gazebo simulator, a physics-engine-based platform that provides more realistic outcomes than traditional numerical simulations by accounting for various physical phenomena.

The remainder of this paper is organized as follows: Section II describes the system, Section III presents the simulation results, and the final section concludes the paper and summarizes the contributions of this work.

II. System Description

A. Omnidirectional Aerial Manipulator Dynamics

The generalized dynamical model of an aerial manipulator is available in the literature, specifically in [23]- This study focuses on an aerial manipulator with a static robotic arm, simplifying the system dynamics significantly. In this scenario, the aerial manipulator can be described as a 6-DoF flying rigid object. The schematic diagram in Fig. 1 illustrates the actively tilted aerial manipulator. Let F_W be the world frame, F_B be the body reference frame, and F_R be the propellers reference frame. The position of the aerial manipulator is represented by ${}^W p_B = [x_B \ y_B \ z_B]^T$, and its orientation is expressed as ${}^W \eta_B = [\phi_B \ \theta_B \ \psi_B]^T$, denoting roll, pitch, and yaw angles, respectively.

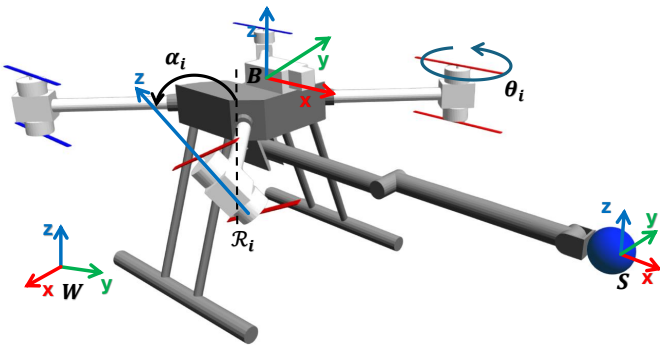

Fig. 1: Omnidirectional actively tilted octarotor equipped with a stick with sensorized circular end-effector.

The dynamic analysis of the actively tilting octarotor with a static robotic arm involves Newton–Euler formulation and algebraic computations [10], [24]. The resulting dynamic equation is

$$B(\zeta)\ddot{\zeta} + C(\zeta, \dot{\zeta})\dot{\zeta} + g(\zeta) = G_B(\zeta)u_B, \tag{1}$$

where $\zeta \in \mathbb{R}^6 \triangleq \left[{}^W p_B{}^T \ {}^W \eta_B{}^T\right]^T$ represents the six-dimensional pose of the UAV in F_W, $g(\zeta) \in \mathbb{R}^6$ is the gravity force vector, and $B(\zeta) \in \mathbb{R}^{6\times 6}$ is the inertia matrix represented as

$$B(\zeta) = \begin{bmatrix} mI_{3\times 3} & 0_{3\times 3} \\ 0_{3\times 3} & D\left({}^W \eta_B\right) \end{bmatrix}$$

with $I_{3\times 3}$ and $0_{3\times 3}$ denoting the identity and zero matrices of the specified dimensions, respectively, $D({}^W \eta_B) \in \mathbb{R}^{3\times 3}$ the inertia matrix of the angular part, and m the total UAV mass. Moreover, $D\left({}^W \eta_B\right) = E\left({}^W \eta_B\right)^T J_B E\left({}^W \eta_B\right)$, where J_B is the inertia tensor of the air-frame and $E(\eta_B) \in \mathcal{SO}(3)$ is a rotation matrix [24]. The matrix $C(\zeta, \dot{\zeta})$ represents the centrifugal and Coriolis forces, and it is given by

$$C(\zeta, \dot{\zeta}) = \begin{bmatrix} 0_{3\times 3} & 0_{3\times 3} \\ 0_{3\times 3} & \begin{array}{c} E({}^W \eta_B)^T S_\times \left(E({}^W \eta_B){}^W \dot{\eta}_B\right) J_b E({}^W \eta_B) \\ + E({}^W \eta_B)^T J_b \dot{E}({}^W \eta_B) \end{array} \end{bmatrix}$$

where $S_\times$ represents the skew-symmetric operator. In addition, $G_B(\zeta) = \text{blockdiag}\left(R({}^W \eta_B), E({}^W \eta_B)\right)$, with $R({}^W \eta_B) \in \mathcal{SO}(3)$ denoting the rotation matrix from F_W to F_B [24].

B. Control Allocation

The control allocation problem consists in finding the rotors speed $\Omega \in \mathbb{R}^8$ and tilt angles $\alpha \in \mathbb{R}^4$ satisfying $u_B = \begin{bmatrix} u_f^{B\,T} & u_\tau^{B\,T} \end{bmatrix} = A(\alpha)\Omega^2$. The mapping between the control inputs and the rotors' angular velocities is handled by

the allocation matrix $A \in \mathbb{R}^{6\times 8}$. Consider again Fig. 1, the position ${}^{B}p_{R_i} \in \mathbb{R}^3$ and orientation ${}^{B}R_{R_i}(\alpha_i(t)) \in SO(3)$ of each rotor's coordinate frame in F_B are

$$ {}^{B}p_{R_i} = \begin{bmatrix} x_{R_i} & y_{R_i} & z_{R_i} \end{bmatrix}^T = lR_z(\chi_i)\mathbf{e}_1 \tag{2} $$

$$ {}^{B}R_{R_i}(\alpha_i(t)) = R_z(\chi_i)R_x(\alpha_i(t)) \tag{3} $$

with $i = 1, 2, 3, 4$ denoting the rotor number, l represents the scalar constant length of each UAV's boom, $\mathbf{e}_1 = [1\ 0\ 0]^T$, $\alpha_i(t)$ is the variable tilting angle. In addition, the total thrust and the torques resulting from the actuation are described as

$$ T_i \in \triangleq k_f\omega_i^2 \tag{4} $$

$$ \tau_{d_{R_i}} \triangleq k_\tau\omega_i^2 \tag{5} $$

where k_f and k_τ are the motors coefficients and $\omega_i \in \mathbb{R}$ is the $i-$th rotor angular velocity. The allocation matrix is a non-linear function of the current tilt angles vector α.

Hence, each propeller exerts the forces $f_{R_i} \in \mathbb{R}^3$ and torques $\tau_{R_i} \in \mathbb{R}^3$ according to its position and orientation as follows

$$ f_{R_i} = T_i {}^{B}R_{R_i}(\alpha_i(t))\mathbf{e}_3 \tag{6} $$

$$ \begin{aligned} \tau_{R_i} = &\left[{}^{B}p_{R_i} \times T_i {}^{B}R_{R_i}(\alpha_i(t))\right] \\ &+ \left[(-1)^{i-1}\sigma T_i {}^{B}R_{R_i}(\alpha_i(t))\mathbf{e}_3\right] \end{aligned} \tag{7} $$

where $\sigma = k_f/k_\tau$ and $\mathbf{e}_3 = [0\ 0\ 1]^T$. Notice that the control wrench $u_B \in \mathbb{R}^6$ can be split into control forces $u_f^B \in \mathbb{R}^3$ and control torques $u_\tau^B \in \mathbb{R}^3$, which are related to the propeller forces and torques by

$$ u_B = \begin{bmatrix} u_f^{B^T} & u_\tau^{B^T} \end{bmatrix}^T = \begin{bmatrix} \sum_{i=1}^4 f_{R_i}^T & \sum_{i=1}^4 \tau_{R_i}^T \end{bmatrix}^T. \tag{8} $$

Therefore, from (6), (7), and (8) the following relation can be obtained $u_B = k_f\Lambda\Omega$, where $\Lambda \in \mathbb{R}^{6\times 16}$ is the allocation matrix which can be expressed as $\Lambda \in \mathbb{R}^{6\times 16} = \begin{bmatrix} A_1 & A_2 \end{bmatrix}$, where $A_1 \in \mathbb{R}^{6\times 8}$ can be written as

$$ A_1 = \begin{bmatrix} 0 & 0 & 0 & 0 & \frac{1}{\sqrt{2}} & \frac{1}{\sqrt{2}} & -\frac{1}{\sqrt{2}} & -\frac{1}{\sqrt{2}} \\ 0 & 0 & 0 & 0 & -\frac{1}{\sqrt{2}} & \frac{1}{\sqrt{2}} & \frac{1}{\sqrt{2}} & -\frac{1}{\sqrt{2}} \\ 1 & 1 & 1 & 1 & 0 & 0 & 0 & 0 \\ \frac{l}{\sqrt{2}} & \frac{l}{\sqrt{2}} & -\frac{l}{\sqrt{2}} & -\frac{l}{\sqrt{2}} & \frac{\sigma}{\sqrt{2}} & -\frac{\sigma}{\sqrt{2}} & -\frac{\sigma}{\sqrt{2}} & \frac{\sigma}{\sqrt{2}} \\ -\frac{l}{\sqrt{2}} & \frac{l}{\sqrt{2}} & \frac{l}{\sqrt{2}} & -\frac{l}{\sqrt{2}} & -\frac{\sigma}{\sqrt{2}} & -\frac{\sigma}{\sqrt{2}} & \frac{\sigma}{\sqrt{2}} & \frac{\sigma}{\sqrt{2}} \\ \sigma & -\sigma & \sigma & -\sigma & -l & -l & -l & -l \end{bmatrix} \tag{9} $$

Whereas $A_2 \in \mathbb{R}^{6\times 8}$ can be written as

$$ A_2 = \begin{bmatrix} 0 & 0 & 0 & 0 & -\frac{1}{\sqrt{2}} & -\frac{1}{\sqrt{2}} & \frac{1}{\sqrt{2}} & \frac{1}{\sqrt{2}} \\ 0 & 0 & 0 & 0 & \frac{1}{\sqrt{2}} & -\frac{1}{\sqrt{2}} & -\frac{1}{\sqrt{2}} & \frac{1}{\sqrt{2}} \\ -1 & -1 & -1 & -1 & 0 & 0 & 0 & 0 \\ -\frac{l}{\sqrt{2}} & -\frac{l}{\sqrt{2}} & \frac{l}{\sqrt{2}} & \frac{l}{\sqrt{2}} & -\frac{\sigma}{\sqrt{2}} & \frac{\sigma}{\sqrt{2}} & \frac{\sigma}{\sqrt{2}} & -\frac{\sigma}{\sqrt{2}} \\ \frac{l}{\sqrt{2}} & -\frac{l}{\sqrt{2}} & -\frac{l}{\sqrt{2}} & \frac{l}{\sqrt{2}} & \frac{\sigma}{\sqrt{2}} & \frac{\sigma}{\sqrt{2}} & -\frac{\sigma}{\sqrt{2}} & -\frac{\sigma}{\sqrt{2}} \\ -\sigma & \sigma & -\sigma & \sigma & l & l & l & l \end{bmatrix} \tag{10} $$

and $\Omega \in \mathbb{R}^{16} \triangleq \begin{bmatrix} T_{11_z} & T_{12_z} & T_{13_z}, & T_{14_z} & T_{11_{xy}} & T_{12_{xy}} & T_{13_{xy}} & T_{14_{xy}} & T_{21_z} & T_{22_z} & T_{23_z} & T_{24_z} & T_{21_{xy}} & T_{22_{xy}} & T_{23_{xy}} & T_{24_{xy}} \end{bmatrix}^T$. Finally, it is possible to map any control wrench u_B to the required rotor speeds and tilting angles of the omnidirectional quadrotor using

$$ \Omega = \Lambda^+ u_B, \tag{11} $$

$$ T_{i_j} = \sqrt{T_{ij_z}^2 + T_{ij_{xy}}^2} \tag{12} $$

$$ \omega_{i_j} = \sqrt{\frac{T_{i_j}}{k_f}} \tag{13} $$

and

$$ \alpha_i(t) = tan^{-1}\left(\frac{T_{ij_z}}{T_{ij_{xy}}}\right) \tag{14} $$

where Λ^+ denotes the Moore-Penrose pseudoinverse of Λ.

C. Controller Design

In this work, we employ the hybrid force/motion controller, a widely used direct force control technique that enables the simultaneous regulation of both contact wrench and end-effector motion [25]. In the context of aerial manipulators, hybrid force and motion control has been effectively implemented using a parallel configuration. In this approach, force control for managing contact and position control for governing motion are handled independently, tailored for constrained and free-flight environments, respectively [26]. The proposed hybrid force/motion controller is presented in [10] as

$$ \begin{cases} u_B = & (I_{6\times 6} - S)\left[K_p \text{tanh}\left(\tilde{\boldsymbol{\zeta}}\right) + K_i \text{tanh}\left(\xi\right)\right] + K_v\dot{\tilde{\zeta}} \\ & + S\left[K_f\tilde{f} + K_j\varphi\right] \\ \dot{\xi} = & \tilde{\zeta} \\ \dot{\varphi} = & \tilde{f} \end{cases} \tag{15} $$

where $\tilde{\zeta} \in \mathbb{R}^6 \triangleq \zeta^d - \zeta$ is the pose error, defined as the difference between the desired pose ζ^d (a constant vector) and the actual pose ζ. Similarly, $\tilde{f} \in \mathbb{R}^6 \triangleq f^d - f$ represents the force error, defined as the difference between the desired force f^d (also a constant vector) and the actual force f. Moreover, the terms $K_p,\ K_i,\ K_v,\ K_f,\ K_j \in \mathbb{R}^{6\times 6}$ are diagonal matrices with positive values, serving as control gains. The matrix $S \in \mathbb{R}^{6\times 6}$ is a switching matrix consisting of zeros and ones, used to designate which axes are force-controlled. Since the objective of this work is to apply a sustained horizontal force along the x_B axis. The switching matrix is selected as $S = \text{diag}(1, 0, 0, 0, 0, 0)$ once the aerial manipulator reaches the desired application point $x_0 \in \mathbb{R}$. Consequently, the force control along the specified axis is governed by this configuration as

$$ \begin{cases} u_{B_x} = & k_{f_x}\tilde{f}_x + k_{j_x}\varphi_x + k_{v_x}\dot{\tilde{\zeta}}_x \\ \dot{\varphi}_x = & \tilde{f}_x \end{cases} \tag{16} $$

where each term $\cdot_x$ represents the scalar component along the $x-$axis of the corresponding vector from equation (15). The constant $k_{f_x},\ k_{j_x},\ k_{v_x}$ are positive value, specifically located in the first entry of the matrix $K_f,\ K_j$ and K_v, respectively.

III. Physics-engine Based Simulation Results

This section outlines the experimental setup used to validate the proposed system. The Gazebo simulator, a physics-engine-based simulation environment, was employed to assess system performance. Gazebo's dynamic 3D simulation produces results that closely mirror real-world experimental outcomes, providing a reliable platform for evaluating the system's capabilities.

A. 3D Simulation set up

The end-effector of the aerial manipulator is modeled as a spherical ball using the URDF (Unified Robot Description Format) syntax. This design allows the end-effector to slide smoothly on surfaces with minimal friction. The simulation environment, constructed in Gazebo, is depicted in Fig. 6. In the environment, a static fixed cart like base of heavy mass of 20 kg is created, which is placed at $(3.0, 0.0, 0.0)$, with four fixed wheel type supports, on the ground. The static fixed base is like a rectangular box with dimensions of 1.2 , (length), 0.6 m (width), and 0.2 m (height), where the visual geometry and collision match these dimensions. A cupboard like rigid heavy box of mass 20 kg is positioned on the top of the cart base with a pose of $(3, 0, 0.7)$ m, with 0.7 m off the ground. The cupboard like heavy box is not static and can be moved or rotated while applying very high force. A box with dimensions of 1.0 m (length), 0.5 m (width), and 1.5 m (height) depict the cupboard. Supportive grey-colored strips act as reinforcing structures around the cupboard-like box, placed at each corner and running horizontally along the top and bottom. This setup is designed to move and rotate freely within the Gazebo simulation environment.

B. Simulation results

The implementation of the proposed setup was achieved using three main programs. The hybrid force/position controllers were developed in C++, while the force controller and navigation algorithms were implemented in Python. Communication between the controller script and the aerial manipulator in the virtual Gazebo environment was managed through ROS. Table I presents the parameters of the allocation matrix and dynamics of the actively tilting octarotor. A force sensor was integrated into the circular ball end-effector to measure the applied interaction force. Various experiments were conducted to validate the overall system.

TABLE I: Parameters of the actively tilting octarotor dynamics and allocation matrix.

Parameter	Value
m	$6.3833\,\text{kg}$
J_b	$\text{diag}(0.1522, 0.1522, 0.1841)\,\text{kg m}^2$
g	$9.81\,\text{m/s}^2$
l	$0.183847763\,\text{m}$
k_f	8.54858×10^{-5}
k_τ	1.75×10^{-4}
k_{f_x}	0.01
k_{j_x}	0.005

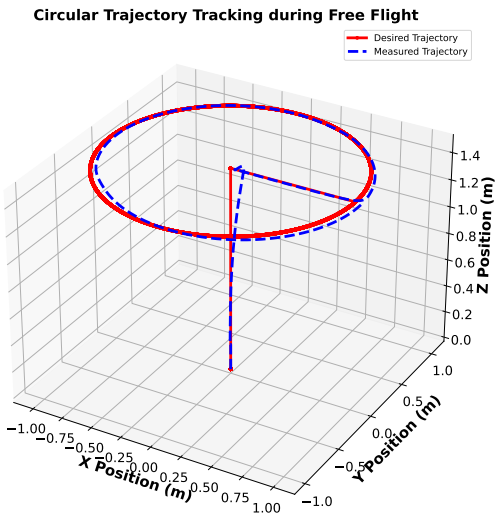

Fig. 2: Circular trajectory tracking with free flight of the aerial manipulator.

1) Circular Trajectory Tracking: In Fig. 2, an experiment is performed where the aerial manipulator is tracking the circular trajectory with free flight. The $3D$ plot in Fig. 2 shows that the aerial manipulator perfectly tracks the circular trajectory, demonstrating the system's satisfactory performance. For this experiment, the aerial manipulator is required to fly 1.5 m along the z-axis while maintaining zero displacement along the x and y axes, then follow a circular trajectory of radius 1 m in the xy-plane. The roll, pitch, and yaw angles are depicted in Fig. 3. A comparison of the desired position and measured positions x, y and z coordinates during the circular trajectory are presented in Fig. 4. Besides, the error between these positions are plotted in the box-plots in Fig. 5, where the height of each box represents the spread of errors, and the whiskers indicate the range of extreme error values. This simulation demonstrates the manipulator's capability to track a circular path accurately, showcasing the efficiency of the control system in maintaining trajectory in the free-flight phase.

2) Rotating a Rigid Heavy Mass: Another set of simulations was performed to rotate a heavy rigid mass of 20 kg by pushing on one side while applying a higher horizontal sustained force. The whole set-up is shown in Fig. 6. Initially, in Fig. 6(a), the aerial manipulator is at ground with position (0,0,0), then take a flight toward the target, approaching the target of a heavy rigid mass before making a physical contact is shown in Fig. 6(b). The manipulator's approach to the target ensures that it reaches the intended position stably before exerting any force, which is crucial for controlled physical interactions. The aerial manipulator reached the target heavy mass at position $(x = 2.3, y = 0, z = 1)$ m. It then slide along the $y-axis$ by 0.4 m to position itself on one side of the heavy

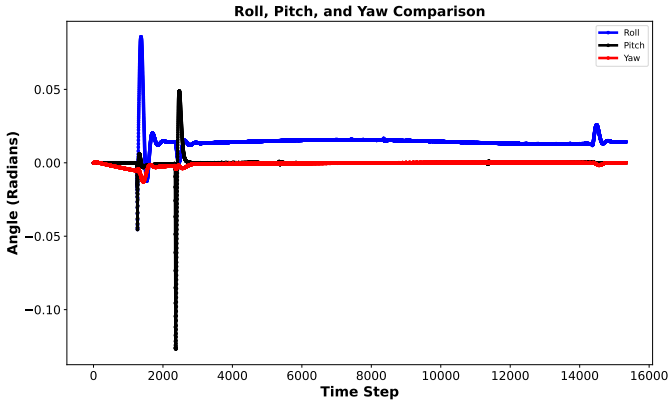

Fig. 3: Roll, pitch and yaw of the circular trajectory tracking while in free flight.

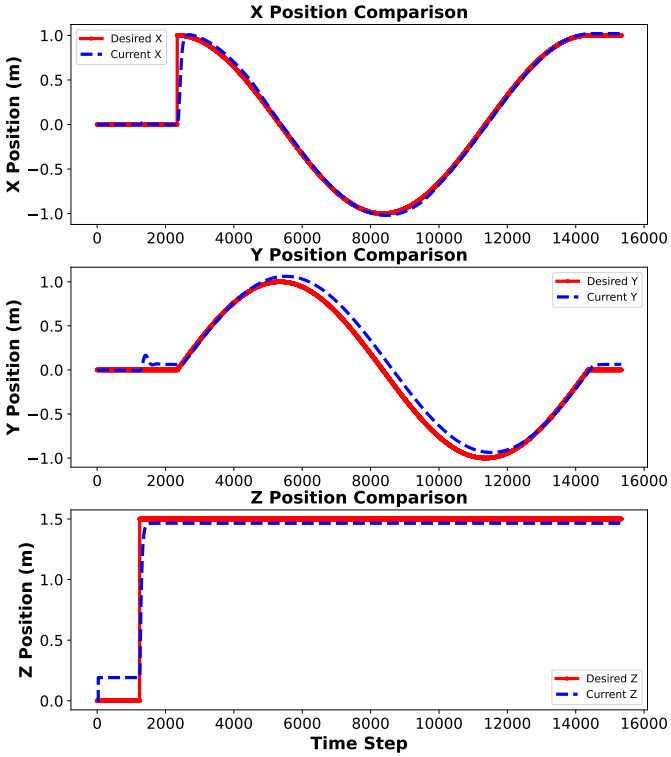

Fig. 4: Comparison of the aerial manipulator position x, y and z with the desired position x, y and z in the circular trajectory.

box, creating a larger moment arm, which helps to generate more rotation, depicted in Fig. 7(a). At this stage, the controller is switched from position to force controller and implementing a sustained horizontal force starting from 1 N and increasing step by step according to the command. Increasing the force from 1 N, 2 N, and 4 N are shown in Fig. 7(b), where there is less rotation because of less force. As the force increases beyond 4 N, the rotation becomes more significant as presented in Fig. 7(c), showcasing the system's capacity to exert controlled forces during manipulation. Overall, in Fig. 7,

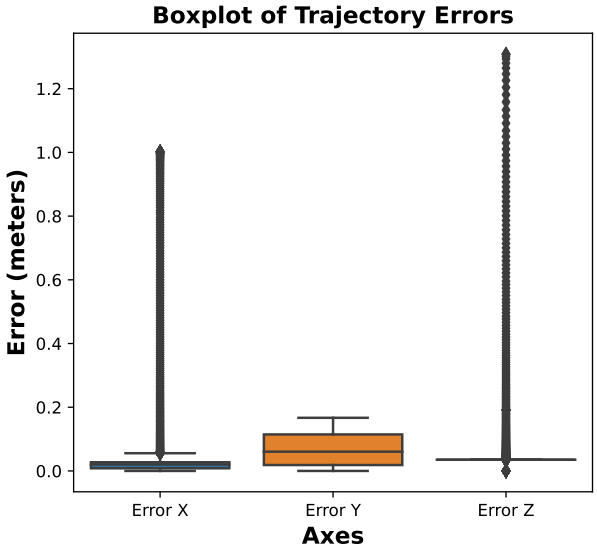

Fig. 5: Box-plots of the error between the position x, y and z with the desired position x, y and z in the circular trajectory.

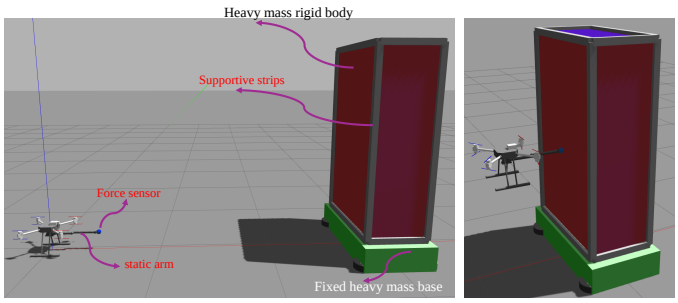

a. Experiment Environment: Aerial manipulator is on ground in front of the heavy rigid mass

b. Aerial manipulator reached the target before the contact

Fig. 6: Aerial manipulator environment and reaching the target before contact

the stages of contact and rotation are depicted, indicating the efficiency and control precision of the aerial manipulator while interacting with heavy masses. A brief video showing how the experiments were put into effect is available at https://youtu.be/4lFarHcHTWI.

The 3 D plot in Fig. 8 illustrates the actual and desired trajectories of the aerial manipulator while rotating a heavy object by applying force. In this case study, the aerial manipulator smoothly follows the desired trajectory before making contact and sliding to one side of the heavy object. However, when switched to force control and applying force along the x-axis, the aerial manipulator is not expected to reach the desired values along the x- and y-axis, as it is focused on applying force to rotate the heavy object. In Fig. 8, it clearly demonstrates that initially, the actual trajectory closely follows the desired trajectory before contact. After switching to force control, with a small force of 1 N, there is only a slight difference between the desired and actual trajectories. However, as the applied

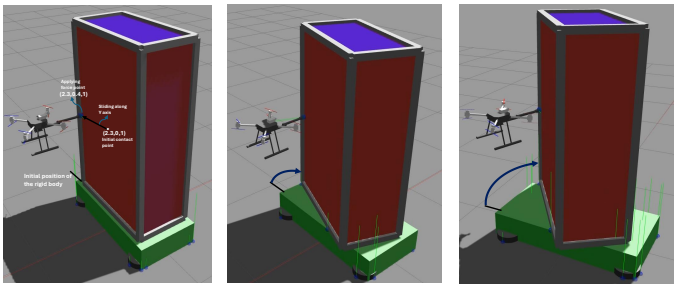

a. Aerial manipulator is in contact with heavy rigid mass, rotating from its one side

b. Rotating while applying less than 4N force

c. Rotating while applying more than 4N force

Fig. 7: Rotating a heavy rigid mass while applying horizontal force.

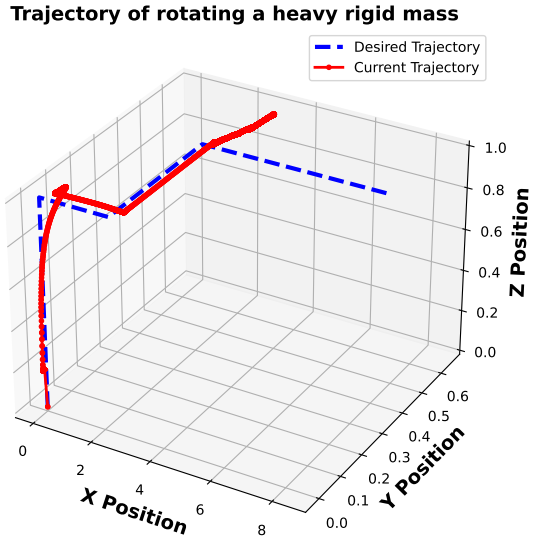

Fig. 8: Trajectory tracking while rotation of heavy mass by applying a sustained higher force.

force increases, the difference grows. This occurs because the drone is no longer moving freely; it is pushing the box to rotate from the corner. This difference reflects the magnitude of the applied force. The aerial manipulator applied up to 8 N of force, which was measured by the force sensor located at the tip of the end effector. Overall, Fig. 8 shows that the the aerial manipulator is very stable. There is no significant change along the z-axis, indicating that the aerial manipulator is maintaining a constant altitude during flight. Figure 9 shows the plots of the desired force and the applied measured force of 1 N, 2 N, 4 N, 6 N, and 8 N while pushing to rotate the heavy rigid mass, using the proposed controller, where it can be appreciated that the force is regulated, with some oscillations but correctly, up to 8 N. Whereas the error between the desired force and applied measured force are presented in Fig. 10.

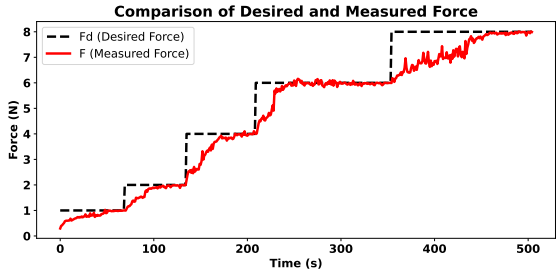

Fig. 9: Desired and measured force during rotating the heavy rigid object.

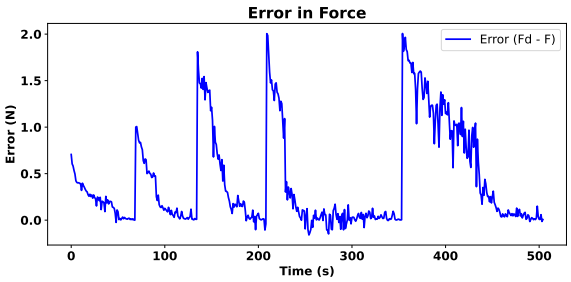

Fig. 10: Error between the desired and measured force.

IV. Conclusions

In this paper, we presented a comprehensive framework for the control and operation of an omnidirectional actively tilted aerial manipulator designed to push and rotate a heavy rigid body. The system leverages the tilting capabilities of the rotors, enabling precise horizontal force application, which is critical for APhI tasks. Simulated experiments in the Gazebo physics engine demonstrated the system's ability to track circular trajectories and rotate heavy objects, validating both the hybrid force/position controller and the overall manipulator architecture. The results showed a high degree of accuracy in trajectory tracking during free-flight maneuvers, with minimal positional errors. Additionally, the system successfully rotated a 20 kg rigid mass with controlled force application, highlighting the force controller's effectiveness and the system's robustness. The simulations also underscored the stability of the aerial manipulator, even during the transition from position to force control, ensuring safe and controlled interaction with the environment.

Future work will focus on implementing this framework in real-world scenarios and refining the control strategies to handle more dynamic and unpredictable environments.

References

[1] X. Meng, Y. He, and J. Han, "Survey on aerial manipulator: System, modeling, and control," *Robotica*, vol. 38, no. 7, pp. 1288–1317, 2020.

[2] I. Ahmad, M. Liaquat, F. M. Malik, H. Ullah, and U. Ali, "Variants of the sliding mode control in presence of external disturbance for quadrotor," *IEEE Access*, vol. 8, pp. 227810–227824, 2020.

[3] A. Raza, F. M. Malik, R. Khan, N. Mazhar, H. Ullah, and N. Ahmed, "Sliding mode control-based autonomous control of a tri-rotor unmanned aerial vehicle," *Guidance, Navigation and Control*, vol. 1, no. 03, p. 2150013, 2021.

[4] M. Ibrahim, H. Ullah, and A. Rasheed, "Vision-based autonomous tracking control of unmanned aerial vehicle," in *2020 IEEE 23rd International Multitopic Conference (INMIC)*, pp. 1–6, IEEE, 2020.

[5] K. Bodie, M. Brunner, M. Pantic, S. Walser, P. Pfändler, U. Angst, R. Siegwart, and J. Nieto, "Active interaction force control for contact-based inspection with a fully actuated aerial vehicle," *IEEE Transactions on Robotics*, vol. 37, no. 3, pp. 709–722, 2020.

[6] A. Ollero, M. Tognon, A. Suarez, D. Lee, and A. Franchi, "Past, present, and future of aerial robotic manipulators," *IEEE Transactions on Robotics*, vol. 38, no. 1, pp. 626–645, 2021.

[7] M. Tognon, H. A. T. Chávez, E. Gasparin, Q. Sablé, D. Bicego, A. Mallet, M. Lany, G. Santi, B. Revaz, J. Cortés, *et al.*, "A truly-redundant aerial manipulator system with application to push-and-slide inspection in industrial plants," *IEEE Robotics and Automation Letters*, vol. 4, no. 2, pp. 1846–1851, 2019.

[8] F. Ruggiero, V. Lippiello, and A. Ollero, "Aerial manipulation: A literature review," *IEEE Robotics and Automation Letters*, vol. 3, no. 3, pp. 1957–1964, 2018.

[9] J. Aleotti, G. Micconi, S. Caselli, G. Benassi, N. Zambelli, M. Bettelli, and A. Zappettini, "Detection of nuclear sources by uav teleoperation using a visuo-haptic augmented reality interface," *Sensors*, vol. 17, no. 10, p. 2234, 2017.

[10] H. Ullah, S. D'Angelo, F. Ruggiero, V. Lippiello, and S. M. O. Soto, "Horizontal sustained force delivery with an aerial manipulator using hybrid force/position control," in *2024 25th International Carpathian Control Conference (ICCC)*, pp. 1–5, IEEE, 2024.

[11] M. Á. Trujillo, J. R. Martínez-de Dios, C. Martín, A. Viguria, and A. Ollero, "Novel aerial manipulator for accurate and robust industrial ndt contact inspection: A new tool for the oil and gas inspection industry," *Sensors*, vol. 19, no. 6, p. 1305, 2019.

[12] R. Rashad, J. Goerres, R. Aarts, J. B. Engelen, and S. Stramigioli, "Fully actuated multirotor uavs: A literature review," *IEEE Robotics & Automation Magazine*, vol. 27, no. 3, pp. 97–107, 2020.

[13] G. Nava, Q. Sablé, M. Tognon, D. Pucci, and A. Franchi, "Direct force feedback control and online multi-task optimization for aerial manipulators," *IEEE Robotics and Automation Letters*, vol. 5, no. 2, pp. 331–338, 2020.

[14] A. Praveen, X. Ma, H. Manoj, V. L. Venkatesh, M. Rastgaar, and R. M. Voyles, "Inspection-on-the-fly using hybrid physical interaction control for aerial manipulators," 2020.

[15] M. Ryll, G. Muscio, F. Pierri, E. Cataldi, G. Antonelli, F. Caccavale, D. Bicego, and A. Franchi, "6d interaction control with aerial robots: The flying end-effector paradigm," *The International Journal of Robotics Research*, vol. 38, no. 9, pp. 1045–1062, 2019.

[16] L. Peric, M. Brunner, K. Bodie, M. Tognon, and R. Siegwart, "Direct force and pose nmpc with multiple interaction modes for aerial push-and-slide operations," in *2021 IEEE International Conference on Robotics and Automation (ICRA)*, pp. 131–137, 2021.

[17] M. Tognon, H. A. T. Chávez, E. Gasparin, Q. Sablé, D. Bicego, A. Mallet, M. Lany, G. Santi, B. Revaz, J. Cortés, and A. Franchi, "A truly-redundant aerial manipulator system with application to push-and-slide inspection in industrial plants," *IEEE Robotics and Automation Letters*, vol. 4, no. 2, pp. 1846–1851, 2019.

[18] S. M. Orozco-Soto, E. Cuniato, J. Cacace, M. Selvaggio, F. Ruggiero, V. Lippiello, and B. Siciliano, "Aerial manipulator interaction with the environment," in *Control of Autonomous Aerial Vehicles: Advances in Autopilot Design for Civilian UAVs*, pp. 319–347, Springer, 2023.

[19] B. Siciliano, L. Sciavicco, L. Villani, and G. Oriolo, *"Robotics: Modelling, Planning and Control"*. Springer, 2009.

[20] K. M. Lynch and F. C. Park, *"Modern Robotics: Mechanics, Planning and Control"*. Cambridge University Press, 2017.

[21] D. Lee, H. Seo, I. Jang, S. J. Lee, and H. J. Kim, "Aerial manipulator pushing a movable structure using a dob-based robust controller," *IEEE Robotics and Automation Letters*, vol. 6, no. 2, pp. 723–730, 2020.

[22] D. Lee, H. Seo, D. Kim, and H. J. Kim, "Aerial manipulation using model predictive control for opening a hinged door," in *2020 IEEE International Conference on Robotics and Automation (ICRA)*, pp. 1237–1242, IEEE, 2020.

[23] V. Lippiello and F. Ruggiero, "Cartesian impedance control of a uav with a robotic arm," *IFAC Proceedings Volumes*, vol. 45, no. 22, pp. 704–709, 2012.

[24] S. M. Orozco Soto, F. Ruggiero, and V. Lippiello, "Globally attractive hyperbolic control for the robust flight of an actively tilting quadrotor," *Drones*, vol. 6, no. 12, p. 373, 2022.

[25] L. Villani, "Force control in robotics," in *Encyclopedia of Systems and Control*, pp. 827–833, Springer, 2021.

[26] X. Meng, Y. He, and J. Han, "Hybrid force/motion control and implementation of an aerial manipulator towards sustained contact operations," in *2019 IEEE/RSJ International Conference on Intelligent Robots and Systems (IROS)*, pp. 3678–3683, IEEE, 2019.